Crossing a topological phase transition with a quantum computer

Adam Smith [1,2,3,*] Bernhard Jobst [1] Andrew G. Green,[4] and Frank Pollmann[1,5]

[1]*Department of Physics, T42, Technische Universität München, James-Franck-Straße 1, D-85748 Garching, Germany*
[2]*Blackett Laboratory, Imperial College London, London SW7 2AZ, England, United Kingdom*
[3]*School of Physics and Astronomy, University of Nottingham, Nottingham NG7 2RD, England, United Kingdom*
[4]*London Centre for Nanotechnology, University College London, Gordon Street, London WC1H 0AH, England, United Kingdom*
[5]*Munich Center for Quantum Science and Technology, Schellingstrasse 4, D-80799 München, Germany*

Quantum computers promise to perform computations beyond the reach of modern computers with profound implications for scientific research. Due to remarkable technological advances, small scale devices are now becoming available for use. One of the most apparent applications for such a device is the study of complex many-body quantum systems, where classical computers are unable to deal with the generic exponential complexity of quantum states. Even zero-temperature equilibrium phases of matter and the transitions between them have yet to be fully classified, with topologically protected phases presenting major difficulties. We construct and measure a continuously parametrized family of states crossing a symmetry protected topological phase transition on the IBM Q quantum computers. We present two complementary methods for measuring string order parameters that reveal the transition, and additionally analyze the effects of noise in the device using simple error models. The simulation that we perform is easily scalable and is a practical demonstration of the utility of near-term quantum computers for the study of quantum phases of matter and their transitions.

There are now many approaches being taken to realize universal quantum computers [1], with numerous academic research groups, companies, and governments across the world devoting resources to each. Amongst the most advanced are devices based on trapped ions [2], localized spins in diamond [3] or silicon [4], and superconducting circuits [5,6]. While each has its advantages—such as coherence times, efficient readout, or gate speeds and fidelities—the latter is fast becoming the most adopted approach. Efforts by D-Wave, Google, IBM, and Rigetti, for example, all use superconducting circuits based on Josephson junctions.

Quantum computational technology is still in its infancy, with the state of the art in superconducting qubits consisting of approximately 100 qubits, 99% two-qubit gate fidelities, and coherence times of the order of 100 μs [6]. Fault-tolerant error correction is also currently out of reach, and solutions for quantum memory and networking are not fully developed. They are consequently described as noisy intermediate-scale quantum (NISQ) devices [7]. There are still unanswered questions about the potential utility of NISQ technology and whether there are fundamental obstructions to going beyond this regime. Nevertheless, there has recently been a flurry of proof-of-principle experiments, along with the recent claim

of a demonstrable computational advantage using a quantum computer [8,9]. For example, in the realm of quantum simulation, real quantum devices have been used to find the ground state of small molecules relevant for quantum chemistry [10,11], to measure multiqubit quantum entanglement [12,13], and to simulate nonequilibrium quantum dynamics [14,15]. This list is far from exhaustive and we do not intend to review the rapid progress of the last decade.

As realized at the very inception of quantum computing [16], the study of complex many-body quantum systems could benefit tremendously from this new technology. Generically, these systems require the storage and manipulation of an exponentially large number of parameters on a classical computer. By storing and manipulating the quantum state directly on a quantum computer, it may be possible to reach areas of condensed matter physics that are currently intractable. As a relevant example, there does not yet exist a complete classification of topological phases of matter [17]. The most interesting and least understood phases occur in two or three dimensions and host exotic non-Abelian anyonic quasiparticles [18], and as a result our most powerful numerical techniques begin to break down. Most notably, quantum Monte Carlo suffers from the sign problem, and dimensionality is a problem for tensor network based methods due to increased entanglement and less efficient contraction schemes when compared with one dimension. On a quantum computer we can avoid classically storing the quantum state, perform sign-problem free computations, and work directly with two-dimensional quantum circuits, potentially sidestepping some of the issues plaguing current numerical techniques. This approach has recently been successfully demonstrated using

---

*adam.smith1@nottingham.ac.uk

both digital quantum computers [19] and quantum simulators [20].

In this Letter we demonstrate how quantum computers can be used to simulate symmetry protected topological (SPT) phases and the transitions between them. This Letter is structured as follows. In Sec. I we introduce symmetry protected topological phases and the concrete models we will consider. Using connections to matrix product states, we discuss how we can simulate the ground states of these models exactly in the thermodynamic limit on a quantum computer in Sec. I A. We then introduce the two methods we use in Sec. II, and show experimental results from the IBM quantum computers [21]. In Sec. III we then analyze three simple error models to understand the observed experimental results and the differences between the two methods. And finally we close with a discussion in Sec. IV.

I. SETUP

Here, we use the IBM quantum computers to study a SPT phase of matter [22,23]. An SPT phase is one that, as long as certain symmetries are present, is not adiabatically connected to a trivial product state. SPTs cannot be understood in the framework of local order parameters and spontaneous symmetry breaking. Instead they are distinguished by nonlocal string order parameters [24–26]. We consider infinite one-dimensional (1D) spin-$\frac{1}{2}$ chains described by the three parameter Hamiltonian

$$\hat{H} = \sum_i \left[-g_{zz}\, \hat{\sigma}_i^z \hat{\sigma}_{i+1}^z - g_x\, \hat{\sigma}_i^x + g_{zxz}\, \hat{\sigma}_i^z \hat{\sigma}_{i+1}^x \hat{\sigma}_{i+2}^z \right]. \quad (1)$$

This Hamiltonian is symmetric under global spin flips generated by $\prod_i \hat{\sigma}_i^x$ as well as time reversal (complex conjugation). Due to these symmetries the model has a $\mathbb{Z}_2 \times \mathbb{Z}_2^T$ SPT phase, as well as a trivial and a symmetry-broken phase. The phase diagram is shown in Fig. 1 [27,28].

We focus on a one-dimensional path through this phase diagram, corresponding to the black curve in Fig. 1, parametrized as $g_{zz} = 2(1 - g^2)$, $g_x = (1 + g)^2$, and $g_{zxz} = (g - 1)^2$, with tuning parameter g [29]. This path continuously interpolates between the cluster Hamiltonian $\hat{H}_{ZXZ} = 4 \sum_i \hat{\sigma}_i^z \hat{\sigma}_{i+1}^x \hat{\sigma}_{i+2}^z$ for $g = -1$ and the trivial paramagnet with Hamiltonian $\hat{H}_X = -4 \sum_i \hat{\sigma}_i^x$ for $g = 1$. The transition between the trivial and the SPT phase occurs at the tricritical point between the three phases at $g = 0$.

The nontrivial SPT phase can be distinguished using string order parameters [31], which are nonlocal observables of macroscopic length l. In the limit $l \to \infty$, the string order parameters are nonzero in one of the two phases and zero in the other. The string order parameters that we consider are of the form

$$\mathcal{S}^O(g) = \langle \psi | \hat{O}_i \left(\prod_{j=i+2}^{k-2} \hat{\sigma}_j^x \right) \hat{O}'_k | \psi \rangle \quad (2)$$

with $\hat{O}_i = \hat{\sigma}_i^z \hat{\sigma}_{i+1}^y$ and $\hat{O}'_k = \hat{\sigma}_{k-1}^y \hat{\sigma}_k^z$ defining $\mathcal{S}^{ZY}(g)$, and $\hat{O}_i = \hat{O}'_k = \mathbb{1}$ defining $\mathcal{S}^{\mathbb{1}}$. The length of the string, l, is the distance between the first and last Pauli operator. For S^{ZY} and $S^{\mathbb{1}}$ the shortest such string lengths are $l = 5$ and 3, respectively. Along our path parametrized by g, the string order
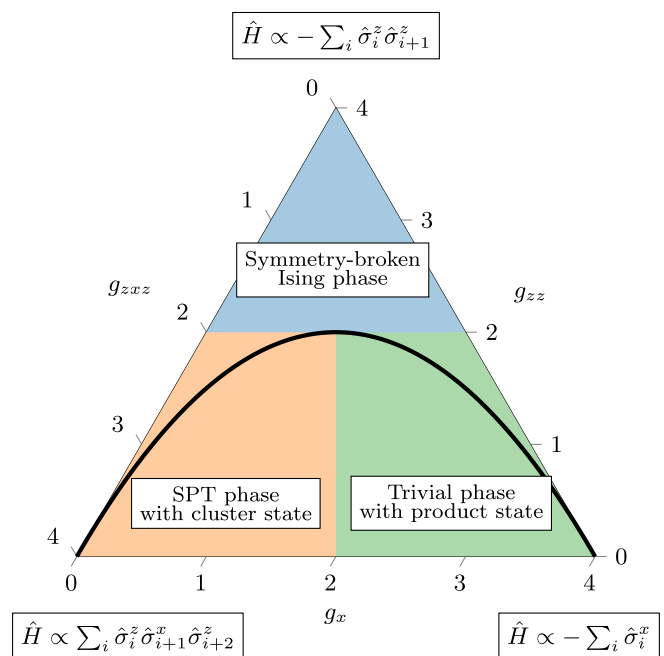

FIG. 1. Phase diagram for the $\mathbb{Z}_2 \times \mathbb{Z}_2^T$ symmetric Hamiltonian in Eq. (1). The green phase is the topologically trivial phase containing the paramagnetic product state, the blue phase is the symmetry-broken phase containing the ferromagnetic ground state of the Ising model, and the orange phase is the SPT phase containing the cluster state. The black curve corresponds to the one-dimensional path with tuning parameter g described in the main text.

parameter $\mathcal{S}^{ZY}(g)$ [resp. $\mathcal{S}^{\mathbb{1}}(g)$] is zero for $g > 0$ ($g < 0$) and equal to $4|g|/(1 + |g|)^2$ for $g < 0$ ($g > 0$). The chosen path has the nice property that the string order parameters are independent of the length of the string and correspond exactly to the values obtained in the thermodynamic limit $l \to \infty$. This property only holds along the black line in Fig. 1 and away from this line we would generically need a macroscopic length l to sharply differentiate the phases.

A. Infinite state as a finite quantum circuit

The ground state of the infinite system can be constructed iteratively by a quantum circuit shown schematically in Fig. 2(a). We can understand this via a connection to infinite matrix product states [32], as outlined in the Supplemental Material [30]. Any observable with finite connected support can equivalently be measured using the finite quantum circuit in Fig. 2(b) [33]. That is, any measurement of the qubits—excluding the unphysical first and last qubits—is identical to the corresponding measurement of the infinite chain. In particular, we measure the same energy density $\mathcal{E} = -2(g^2 + 1)$ and values for the string order parameters. Note that this representation of the ground state is exact and in the thermodynamic limit.

We arrive at the finite circuit in Fig. 2(b) by first viewing a measurement as sandwiching an operator between the quantum circuit (the ket) and the Hermitian conjugate circuit (the bra) as shown in Fig. 3(a). Away from the observable that we are measuring we find circuit elements of the form shown in Fig. 3(b). Below the measured operator these will all cancel
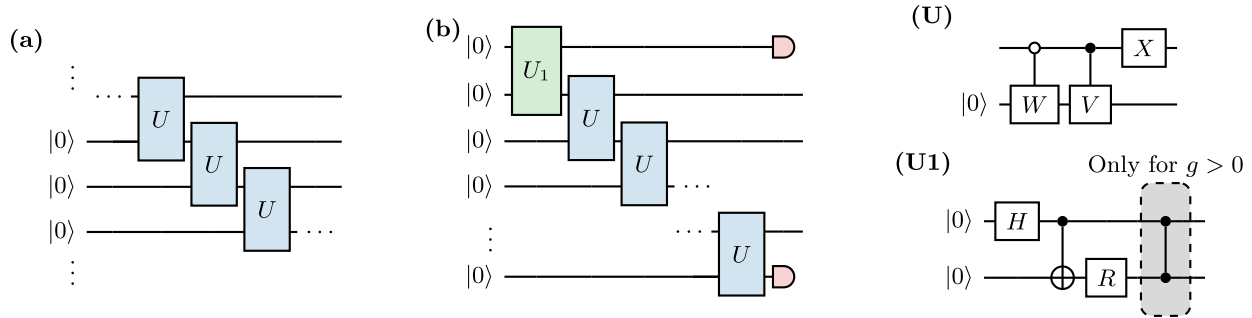
FIG. 2. Quantum circuit construction of the states. (a) Iterative construction of the ground state on an infinite chain. (b) Equivalent finite quantum circuit for measuring observables with finite connected support. Red caps indicate that the end qubits are unphysical and should not be measured. (U) and (U1) are the circuits for the two-qubit gates U and U_1, respectively. X is the Pauli-X gate, and the single qubit gates R, W, and V are specified in the Supplemental Material [30].

due to unitarity. While we cannot do this for the gates above the measurement, we can construct the gate U_1 as a fixed point of the iterative circuit. More explicitly, we can reinterpret the circuit in Fig. 3(b) as a transfer matrix $T_{(\beta\beta'),(\alpha\alpha')}$. The expectation value of the operator in the thermodynamic limit is then determined by the fixed points of the transfer matrix, similar to the thermodynamic treatment of the classical 1D Ising model. Similarly, we can consider the circuit in Fig. 3(c) as a vector $V_{(\alpha\alpha')}$. The unitary U_1 is chosen such that $V_{(\alpha\alpha')}$ is the dominant right eigenvector of $T_{(\beta\beta'),(\alpha\alpha')}$ with eigenvalue 1, i.e., the fixed-point vector under repeated application of the transfer matrix. See Supplemental Material [30] for more details. An alternative way to state the cancellation of the unitary gates below the measurement is that the dominant left eigenvector of the transfer matrix corresponds to the identity.

II. RESULTS

We will consider two methods for measuring the string order parameters on the IBM quantum computers: *direct measurement* and *interferometry*. In the former we rotate all of
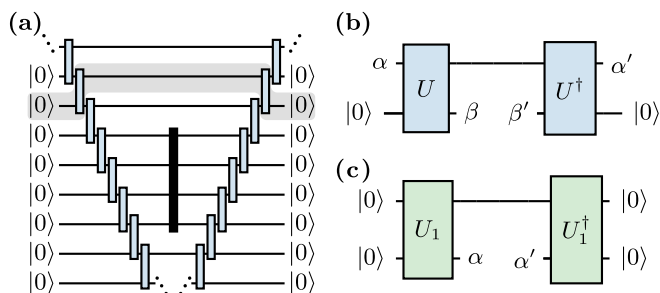

FIG. 3. Elements of the quantum circuit construction. (a) Expectation value of an observable is equivalent to sandwiching the operator (black box) between the state and its conjugate. For the infinite system the corresponding circuit contains a repeating element (highlighted in gray). (b) The repeated circuit element away from the measured observable when computing expectation values. This circuit element can be interpreted as a transfer matrix (see main text). (c) Corresponding fixed-point vector as a quantum circuit.

the relevant qubits to the correct basis and then measure all qubits simultaneously. From these measurements we are able to reconstruct the expectation value of Pauli strings, which allows us to measure the energy and string order parameters. In the latter interferometry experiments, we will instead use an additional ancilla qubit which we will entangle with the qubits that we want to measure the string order parameter on. By measuring only this ancilla qubit at the end we can also extract the string order parameter. Details of the interferometry circuits are given in Sec. II B and the Supplemental Material [30]. Direct measurement requires a shallower circuit and so is less susceptible to gate errors and decoherence. However, interferometry only requires the measurement of a single qubit in contrast to the direct measurement of many, and so will be impacted less by measurement error. We will compare the accuracy of these two methods due to the competition of different sources of error on current devices.

For our simulations we used the 27 qubit IBM Q device codenamed `toronto` on 25 October 2021, which allows the implementation of a universal gate set consisting of arbitrary single qubit rotations and controlled-NOT (CNOT) entangling gates between connected qubits. The decomposition of the circuit shown in Fig. 2 into this gate set is given in the methods section. The spins in our system are mapped to the physical qubits of the quantum computer, with the basis states $\{|\uparrow\rangle = |0\rangle, |\downarrow\rangle = |1\rangle\}$, and we control the devices using the PYTHON qiskit API [34]. To select our subset of N qubits we use a custom procedure described in Ref. [14], which maximizes the average CNOT fidelity, while limiting the readout error and coherence time for the qubits. When using the direct method, we also perform error mitigation on the raw data from the machine using methods provided in qiskit [34], to reduce the impact of readout errors, which we outline in the Supplemental Material [30]. We perform 8192 runs for each circuit and omit error bars in our figures since the statistical error is not significant.

A. Direct measurement

Figure 4 shows the energy density of the state as measured on the IBM device compared with the analytic value, $\mathcal{E} = -2(g^2 + 1)$. We measure the local energies and average over the central qubits excluding the boundary qubits (i.e., $i = 2, \ldots, N - 3$), and show the results measured on subsystems
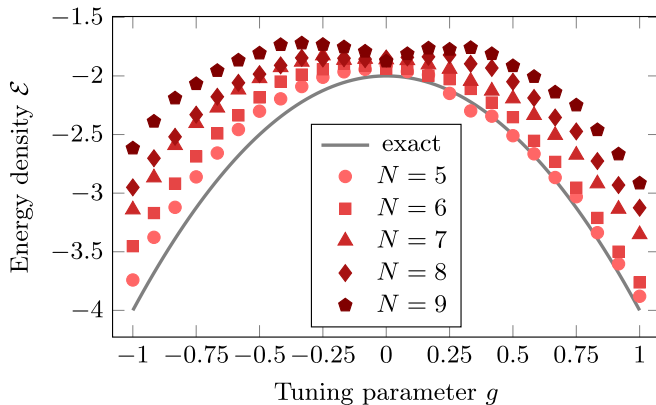
FIG. 4. Average energy density. We measure the local energy of the state using number of qubits $N = 5, 6, 7, 8, 9$. The energy is averaged over the central sites excluding the end qubits. The data from the IBM devices are compared with the analytic result.

of $N = 5, \ldots, 9$ qubits. Despite the discrepancy in the absolute value, the energy obtained from the quantum computer follows nicely the exact functional form indicating proximity to the target state. The difference between the experimental and the exact result can predominantly be attributed to dephasing and measurement error. The former accounts for the change in shape, with a dip around $g = 0$, since it impacts the $\langle \hat{\sigma}_j^x \rangle$ and $\langle \hat{\sigma}_j^z \hat{\sigma}_{j+1}^x \hat{\sigma}_{j+2}^z \rangle$ expectation values but not $\langle \hat{\sigma}_j^z \hat{\sigma}_{j+1}^z \rangle$. Furthermore, we expect the amount of dephasing to scale with the circuit depth and so with N. A demonstration of the effect of dephasing on the energy density is shown in the Supplemental Material [30]. The measurement error on the other hand does not scale with N and accounts for the slight asymmetry between $g < 0$ and $g > 0$, due to the various lengths of the terms in the Hamiltonian.

Next we show the measurements of the two string order parameters in Fig. 5 for lengths $l = 5, 6, 7$ for $\mathcal{S}^{ZY}(g)$, and $l = 3, \ldots, 7$ for $\mathcal{S}^{\mathbb{1}}(g)$, and compare with the analytic results. Especially for the smallest string lengths, we see qualitative agreement between the results from the quantum computer and the exact results. It appears that for small enough sizes we can well approximate the errors in the device by a constant scaling factor. Importantly, the order parameters are only nonzero in one of the two phases, and tend to zero at the phase transition $g = 0$. However, beyond a certain string length, $l \gtrsim 6$, this information is lost and there is no clear transition point.

As we increase the string length in Fig. 5, the accuracy of the results quickly diminishes, even more so than was observed in Fig. 4. This is due to the fact that we are measuring nonlocal operators and both the number of qubits and the length of the operator are increasing. For chains of length $N = 9$ ($l = 7$) we are no longer able to detect the transition, demonstrating the difficulty of constructing and measuring long-range string order in the quantum state due to the current limitations of the quantum computer. Nevertheless, the combination of the measurements of the energy density and the string order parameters confirms that we are able to approximately construct the target states with nontrivial string order on a real quantum computer.
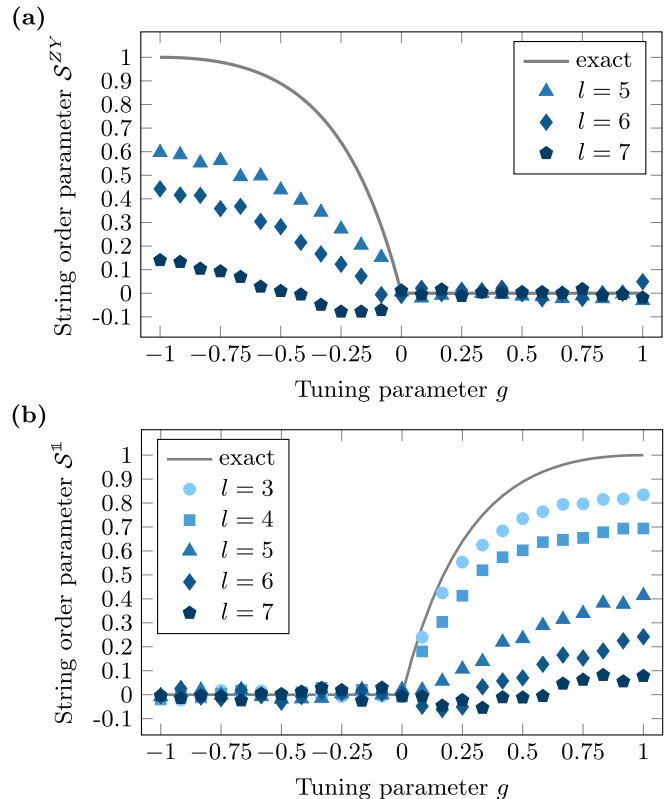
FIG. 5. Identification of the phase transition using direct measurement. (a) Results of the string order parameter $\mathcal{S}^{ZY}(g)$ of length $l = 5, 6, 7$, simulated using number of qubits $N = 7, 8, 9$, respectively. (b) $\mathcal{S}^{\mathbb{1}}(g)$ of length $l = 3, 4, 5, 6, 7$, corresponding to $N = 5, 6, 7, 8, 9$. We compare with the analytic results.

B. Interferometry experiment

We now consider an alternative method to measure the string order parameters on the quantum computer. This method is motivated by Ramsey- or Mach-Zender-type interferometry experiments and is known as a Hadamard test in quantum computing. The circuit diagram is given in Fig. 6. The basic idea is to use an ancilla qubit prepared in an equal weight superposition using a Hadamard gate. We then use a controlled operation that implements the Pauli string $\hat{S}^O$ associated with our string order parameter if the ancilla is in the $|1\rangle$ state. Finally, we apply a Hadamard gate and measure only this ancilla qubit. The expectation value of the ancilla qubit gives the real part of $\langle \psi | \hat{S}^O | \psi \rangle$, which since the Pauli string is Hermitian is equivalent to our string order parameters. We give more details of this method and a decomposition of the circuit into two-qubit gates in the Supplemental Material [30].

In Fig. 7 we show the results from the IBM quantum computer for the interferometry experiments where we see a significant improvement over the results shown in Fig. 5. The quantitative accuracy is improved for all string lengths and a far reduced dependence on the length is observed. In fact, the measured values do not seem to decrease monotonically with increasing string length. This suggests that the fluctuations between these different runs is comparable to or larger than the increased error from the deeper circuit. Importantly the qualitative behavior, including the location of the phase
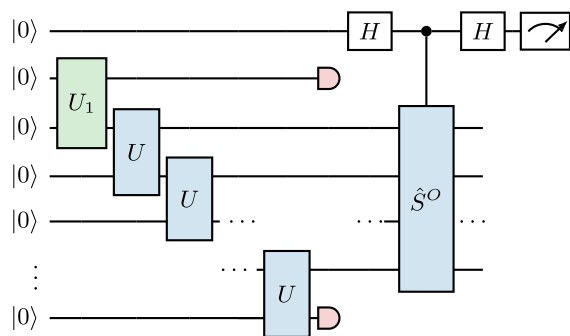
FIG. 6. Interferometry circuit diagram. The quantum circuit used for the interferometry method for measuring string order parameters. The top ancilla qubit is used to perform a controlled unitary that implements the relevant Pauli string in the string order parameter. Measurement of the ancilla qubit is equivalent to the measurement of the string order parameter. Explicit decomposition into elementary gates is provided in the Supplemental Material [30].

transition, is clearly visible for both string order parameters for all string lengths l.

III. ERROR MODELING

In our results from the IBM quantum computers there was a stark contrast in the quality of results obtained by the two different methods. While one used shallow circuits and measured many qubits, the other measured only one qubit at the cost of deeper circuits. Therefore the two methods are impacted differently by the various sources of errors in these quantum devices. In this section we use simple models to analyze the impact of three different sources of errors: measurement error, unitary gate errors, and decoherence. In Fig. 8 we plot the relative error in the string order parameter against the length of the string order parameter and the relevant error rate. The relative error is computed at $g = 0.5$ for $S^{\mathbb{1}}$ and $g = -0.5$ for S^{ZY}.

A. Measurement error

First, let us consider the measurement error. We use a simple model for independent bit flip errors, where during the measurement process there is a probability $\epsilon \in [0, 1]$ that a qubit is flipped. To simulate this process we consider the pure state $|\psi\rangle$ produced by the circuit and construct a vector containing the probabilities of measuring each bit string, i.e., $p_i = |\langle i|\psi\rangle|^2$, where $|i\rangle$ is a computational basis state. We then construct an error matrix M_ϵ, the elements of which are given by

$$\langle i|M_\epsilon|j\rangle = \epsilon^{N_{ij}}(1-\epsilon)^{N-N_{ij}}, \tag{3}$$

where N is the total number of qubits and N_{ij} is the number of bit flips between $|i\rangle$ and $|j\rangle$. As an explicit example, let $|i\rangle = |010011\rangle$ and $|j\rangle = |110010\rangle$, then $N = 6$ and $N_{ij} = 2$. We then apply this matrix to our probability vector to get the new probabilities taking into account measurement error, $\tilde{p}_i = \sum_j [M_\epsilon]_{ij} p_j$. Finally, we can evaluate the string order parameters from these updated probabilities $\tilde{p}_i$. Despite the simplicity of this measurement error model, a similar model
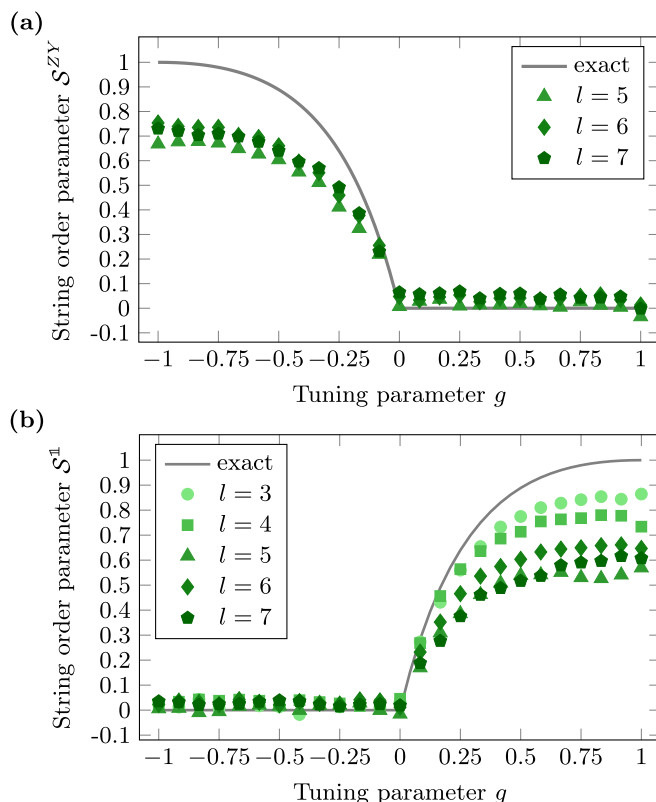

FIG. 7. Identification of the phase transition using interferometry. (a) Results of the string order parameter $\mathcal{S}^{ZY}(g)$ of length $l = 5, 6, 7$, simulated using number of qubits $N = 7, 8, 9$, respectively. (b) $\mathcal{S}^{\mathbb{1}}(g)$ of length $l = 3, 4, 5, 6, 7$, corresponding to $N = 5, 6, 7, 8, 9$. We compare with the analytic results.

is routinely used to perform effective error mitigation and used by ourselves as explained in the Supplemental Material [30].

The results from the measurement error model are shown in Figs. 8(a) and 8(b). The first thing to note is that the relative error of the direct method increases with the length of the string order parameter, but does not for the interferometry method. This is because in the latter we are only ever measuring a single qubit, and so the probability of a measurement error is simply given by ϵ. In contrast, when measuring multiple qubits, errors in any of these qubits affect the string order parameter. Furthermore, this means the direct method is also significantly more sensitive to increasing the probability of bit flip errors, as shown in Fig. 8(b). For the IBM device that we used, the average readout error corresponded to approximately $\epsilon = 0.03$. Our simulations show that this alone could account for approximately a 30% error in the string order parameter for $l = 5$ for the direct method, with even larger errors for $l > 5$.

B. Unitary gate error

The second type of error that we will consider is unitary gate errors. These might correspond to imperfectly calibrated gates or drift in the device that means the intended unitary is not implemented perfectly. For this simulation we assume that single qubit gates are implemented perfectly, but the entangling CNOT gates are subject to random unitary perturbations.
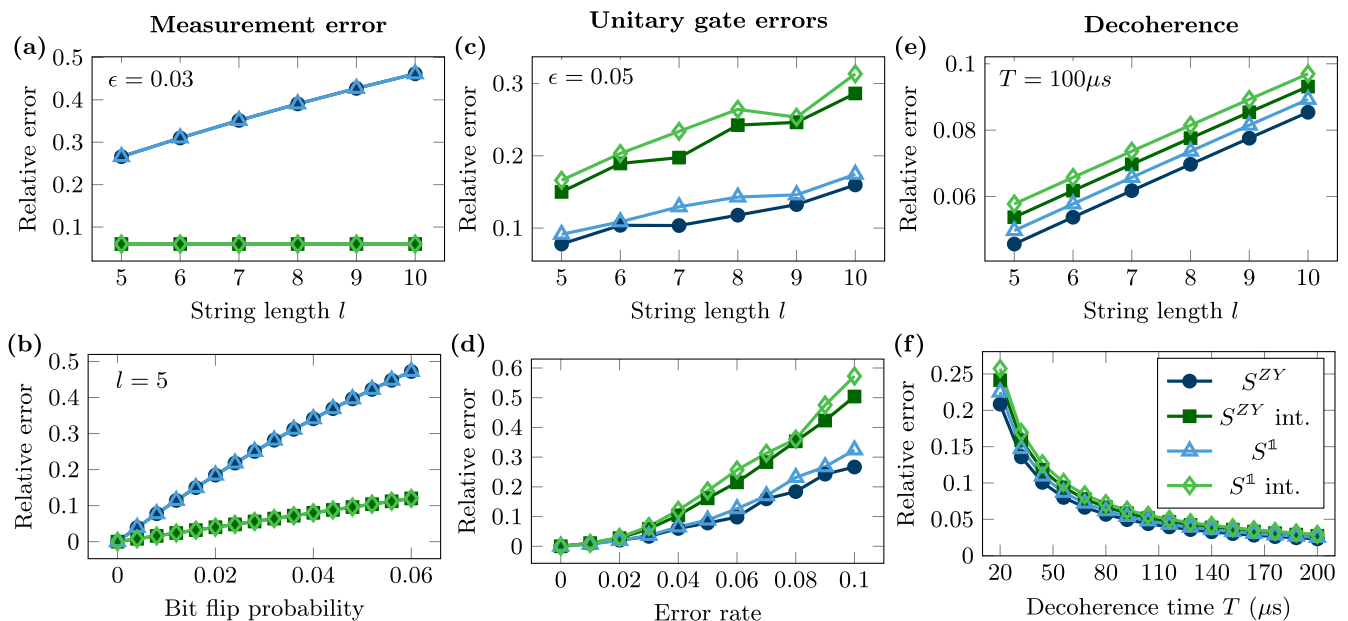
FIG. 8. Relative error for simple error models. Numerical simulations for three simple error models: (a, b) measurement errors as described in Sec. III A, (c, d) unitary gate errors as described in Sec. III B, and (e, f) decoherence due to the polarizing channel as described in Sec. III C. Subfigures (a), (c), and (e) show the dependence of the relative error on string length with bit flip probability 0.03, error rate 0.05, and decoherence time 100 μs, respectively. Subfigures (b), (d), and (f) show the dependence on the relevant error rate for the model for string length $l = 5$. Solid symbols correspond to the relative error of S^{ZY} ($g = -0.5$), and hollow symbols correspond to $S^{\mathbb{1}}$ ($g = 0.5$). Data simulated using the interferometry method are labeled "int." in the legend.

This will be done in the following way:

$$\text{CNOT} \rightarrow \exp[\log(\text{CNOT}) + i\epsilon H], \qquad (4)$$

where $H = (M + M^\dagger)/2$ and M has complex matrix elements drawn from a normal random distribution, and ϵ controls the error rate. Here exp and log refer to matrix exponential and logarithm, respectively. In our simulations we average over 100 realizations of the random gates.

As shown, in Fig. 8(c), the error for both methods now increases as a function of the string length. Furthermore, the interferometry method is now more sensitive to this type of error due to the increased number of gates in the circuit. However, the difference between the two is much less drastic than in the case of measurement errors. Unfortunately, we are not able to quantify the amount of unitary gate error in the IBM quantum computers since it is difficult to disentangle unitary gate errors from other decoherent sources of error.

C. Decoherence

Despite the remarkable amount of isolation achieved to realize current quantum computers, these devices are not perfectly closed systems. As a result, the qubits interact with the environment and will be eventually become decoherent. There are many forms of decoherence that happen in a realistic device but for simplicity we focus only on the depolarizing channel. Furthermore, while the decoherence is in reality happening throughout the implementation of the circuit, as well as state preparation and readout, we will apply the depolarizing channel at once, immediately prior to measurement. While this is certainly an approximation of reality, this model has also been used to effectively mitigate errors on quantum

computers [35], which verifies its approximate validity on current devices.

Concretely, following the application of our quantum circuit we will be in the pure state $|\psi\rangle$ and then the depolarizing channel will result in the mixed state represented by the density matrix

$$\rho = \epsilon \frac{\mathbb{1}}{2^N} + (1 - \epsilon)|\psi\rangle\langle\psi|. \qquad (5)$$

The parameter ϵ controls the amount to which the pure state is mixed with a completely mixed density matrix. The parameter $\epsilon = (1 - e^{-t/T})$, where t is the total time of the circuit and T is the time scale for decoherence. Due to an order of magnitude difference in time scales, we assume single qubit gates are instantaneous whereas CNOT gates are implemented in 425 ns, the average for the IBM quantum computer we used. The total time is then given by the gate time multiplied by the number of asynchronous CNOT gates. The corresponding decoherence time for the device was approximately 100 μs.

The error due to this depolarizing channel appears to scale approximately linearly with the string length l, as shown in Fig. 8(e). This corresponds to the linear increase in circuit depth with l. However, the difference between the direct and interferometry methods is small. This is because these methods only differ by two asynchronous layers of CNOT gates. The rest of the additional CNOT gates can be done in parallel with the gates common to both methods. Additionally, the circuit for $S^{\mathbb{1}}$ measured at $g = 0.5$ has one additional CNOT gate compared with S^{ZX} at $g = -0.5$, the effect of which can also be seen in this figure. In Fig. 8(f) we plot the relative error as a function of the decoherence time, which shows a characteristic exponential behavior.

IV. DISCUSSION

Above we have focused on a particular line through the phase diagram in Fig. 1, which has an especially efficient construction of the ground states. This enabled an exact representation within the limitations of existing devices. In this Letter we have considered a particularly simple path, but our approach is general and potentially provides a genuine advantage to using NISQ devices. In fact, all matrix product states can be constructed in a similar way [33,36] and can be variationally optimized on a quantum computer [33]. Such variational solvers have already been demonstrated in the setting of small molecules [10,11] using variational quantum eigensolvers [37].

It is still an open and interesting problem to find optimal *Ansatz* circuits for variational optimization. A recent work has shown that sequential quantum circuit *Ansätze*—similar to the ones used in this Letter—are efficient "sparse" representations for some quantum ground states and in simulating nonequilibrium dynamics [38]. By directly using the connectivity of the quantum computers it may be possible to go beyond what is accessible with classical numerics in two dimensions with shallow depth (polynomial in system size) quantum circuits. In particular, it is often numerically expensive to compute correlators in higher-dimensional tensor networks. Representing these as quantum circuits [39] will permit considerable speedup in their manipulation and measurement—with a potential exponential advantage in certain circumstances. As a concrete example, there exists a simple representation of topologically ordered string-net models [40] in terms of tensor networks [41,42], that nevertheless remains difficult to deal with numerically.

We demonstrated experimentally on the IBM quantum computers two alternative methods for measuring nonlocal string order parameters. While direct measurement of multiple qubits was highly sensitive to increased string length, the interferometric method gave consistent qualitative agreement to the exact results. By analyzing three simple error models we identified readout errors as those that dominated our results, and so strongly favored the interferometric approach which

required measurement of a single qubit. It is possible that in other quantum computer technologies the extent of measurement and gate errors (either coherent or decoherent) would be reversed and in that case the direct method might be preferred. It is clear that in the NISQ era it is important to understand the sources of error of a particular device and tailor our approach accordingly.

Beyond SPT phases, where we know how to construct the order parameters, we need to find efficient ways of detecting and differentiating different phases. Recent work proposes quantum-hybrid algorithms based on ideas from machine learning and renormalization group [43,44]. These algorithms are scalable and practical to implement on near-term devices. The combination of machine learning tools and quantum hardware is potentially very powerful with many applications [45].

In this Letter we have distinguished two topologically inequivalent phases and identified the transition between them using a real quantum device. We compared two complimentary methods and analyzed their relative accuracy using simple error models. Despite the infancy of the current technology, our Letter clearly demonstrates that near-term NISQ devices can be used as practical tools for the study of condensed matter physics.

[1] M. A. Nielsen and I. L. Chuang, *Quantum Computation and Quantum Information* (Cambridge University, Cambridge, England, 2010)

[2] C. D. Bruzewicz, J. Chiaverini, R. McConnell, and J. M. Sage, Trapped-ion quantum computing: Progress and challenges, Appl. Phys. Rev. **6**, 021314 (2019).

[3] C. E. Bradley, J. Randall, M. H. Abobeih, R. C. Berrevoets, M. J. Degen, M. A. Bakker, M. Markham, D. J. Twitchen, and T. H. Taminiau, A Ten-Qubit solid-state spin register with quantum memory up to one minute, Phys. Rev. X **9**, 031045 (2019).

[4] C. H. Yang, K. W. Chan, R. Harper, W. Huang, T. Evans, J. C. C. Hwang, B. Hensen, A. Laucht, T. Tanttu, F. E. Hudson, K. M. Itoh, A. Morello, S. D. Bartlett, and A. S. Dzurak, Silicon qubit fidelities approaching incoherent noise limits via pulse engineering, Nat. Electron. **2**, 151 (2019).

[5] G. Wendin, Quantum information processing with superconducting circuits: A review, Rep. Prog. Phys. **80**, 106001 (2017).

[6] M. Kjaergaard, M. E. Schwartz, J. Braumüller, P. Krantz, J. I.-J. Wang, S. Gustavsson, and W. D. Oliver, Superconducting qubits: Current state of play, Annu. Rev. Condens. Matter Phys. **11**, 369 (2020).

[7] J. Preskill, Quantum computing in the NISQ era and beyond, Quantum **2**, 79 (2018).

[8] S. Boixo, S. V. Isakov, V. N. Smelyanskiy, R. Babbush, N. Ding, Z. Jiang, M. J. Bremner, J. M. Martinis, and H. Neven, Characterizing quantum supremacy in near-term devices, Nat. Phys. **14**, 595 (2018).

[9] F. Arute, K. Arya, R. Babbush, D. Bacon, J. C. Bardin, R. Barends, R. Biswas, S. Boixo, F. G. S. L. Brandao, D. A. Buell, B. Burkett, Y. Chen, Z. Chen, B. Chiaro, R. Collins, W. Courtney, A. Dunsworth, E. Farhi, B. Foxen, A. Fowler *et al.*, Quantum supremacy using a programmable superconducting processor, Nature (London) **574**, 505 (2019).

[10] A. Kandala, A. Mezzacapo, K. Temme, M. Takita, M. Brink, J. M. Chow, and J. M. Gambetta, Hardware-efficient variational

quantum eigensolver for small molecules and quantum magnets, Nature (London) **549**, 242 (2017).

[11] P. J. J. O'Malley, R. Babbush, I. D. Kivlichan, J. Romero, J. R. McClean, R. Barends, J. Kelly, P. Roushan, A. Tranter, N. Ding, B. Campbell, Y. Chen, Z. Chen, B. Chiaro, A. Dunsworth, A. G. Fowler, E. Jeffrey, E. Lucero, A. Megrant, J. Y. Mutus *et al.*, Scalable quantum simulation of molecular energies, Phys. Rev. X **6**, 031007 (2016).

[12] K. Choo, C. W. von Keyserlingk, N. Regnault, and T. Neupert, Measurement of the Entanglement Spectrum of a Symmetry-Protected Topological State Using the IBM Quantum Computer, Phys. Rev. Lett. **121**, 086808 (2018).

[13] Y. Wang, Y. Li, Z.-Q. Yin, and B. Zeng, 16-qubit IBM universal quantum computer can be fully entangled, npj Quantum Inf. **4**, 46 (2018).

[14] A. Smith, M. S. Kim, F. Pollmann, and J. Knolle, Simulating quantum many-body dynamics on a current digital quantum computer, npj Quantum Inf. **5**, 106 (2019).

[15] F. Tacchino, A. Chiesa, S. Carretta, and D. Gerace, Quantum computers as universal quantum simulators: state-of-art and perspectives, Adv. Quantum Technol. **3**, 1900052 (2020).

[16] R. P. Feynman, Simulating physics with computers, Int. J. Theor. Phys. **21**, 467 (1982).

[17] X.-G. Wen, Choreographed entangle dances: Topological states of quantum matter, arXiv:1906.05983.

[18] C. Nayak, S. H. Simon, A. Stern, M. Freedman, and S. Das Sarma, Non-Abelian anyons and topological quantum computation, Rev. Mod. Phys. **80**, 1083 (2008).

[19] K. J. Satzinger, Y.-Jie Liu, A. Smith, C. Knapp, M. Newman, C. Jones, Z. Chen, C. Quintana, X. Mi, A. Dunsworth, C. Gidney, I. Aleiner, F. Arute, K. Arya, J. Atalaya, R. Babbush, J. C. Bardin, R. Barends, J. Basso, A. Bengtsson *et al.*, and Realizing topologically ordered states on a quantum processor, arXiv:2104.01180.

[20] G. Semeghini, H. Levine, A. Keesling, S. Ebadi, T. T. Wang, D. Bluvstein, R. Verresen, H. Pichler, M. Kalinowski, R. Samajdar, *et al.*, Probing topological spin liquids on a programmable quantum simulator, Science **374**, 1242 (2021).

[21] IBM Quantum. https://quantum-computing.ibm.com/, 2021.

[22] F. Pollmann, A. M. Turner, E. Berg, and M. Oshikawa, Entanglement spectrum of a topological phase in one dimension, Phys. Rev. B **81**, 064439 (2010).

[23] X. Chen, Z. C. Gu, Z. X. Liu, and X. G. Wen, Symmetry protected topological orders and the group cohomology of their symmetry group, Phys. Rev. B **87**, 155114 (2013).

[24] J. Haegeman, D. Pérez-García, I. Cirac, and N. Schuch, Order Parameter for Symmetry-Protected Phases in One Dimension, Phys. Rev. Lett. **109**, 050402 (2012).

[25] F. Pollmann and A. M. Turner, Detection of symmetry-protected topological phases in one dimension, Phys. Rev. B **86**, 125441 (2012).

[26] A. Elben, J. Yu, G. Zhu, M. Hafezi, F. Pollmann, P. Zoller, and B. Vermersch, Many-body topological invariants from randomized measurements, Sci. Adv. **6**, eaaz3666 (2020).

[27] R. Verresen, R. Moessner, and F. Pollmann, One-dimensional symmetry protected topological phases and their transitions, Phys. Rev. B **96**, 165124 (2017).

[28] R. Verresen, N. G. Jones, and F. Pollmann, Topology and Edge Modes in Quantum Critical Chains, Phys. Rev. Lett. **120**, 057001 (2018).

[29] M. M. Wolf, G. Ortiz, F. Verstraete, and J. I. Cirac, Quantum phase transitions in matrix product systems, arXiv:0512180 (2005).

[30] See Supplemental Material at http://link.aps.org/supplemental/10.1103/PhysRevResearch.4.L022020 for additional details on the connection between quantum circuits and MPS, explicit definitions of unitary gates featured in the main text, error mitigation techniques used, details of the interferometry circuits, and additional error modelling.

[31] D. Pérez-García, M. M. Wolf, M. Sanz, F. Verstraete, and J. I. Cirac, String Order and Symmetries in Quantum Spin Lattices, Phys. Rev. Lett. **100**, 167202 (2008).

[32] G. Vidal, Classical Simulation of Infinite-Size Quantum Lattice Systems in One Spatial Dimension, Phys. Rev. Lett. **98**, 070201 (2007).

[33] F. Barratt, J. Dborin, M. Bal, V. Stojevic, F. Pollmann, and A. G. Green, Parallel quantum simulation of large systems on small quantum computers, npj Quantum Inf. **7**, 79 (2021).

[34] G. Aleksandrowicz *et al.*, Qiskit: An Open-source Framework for Quantum Computing (2019).

[35] J. Vovrosh, K. E. Khosla, S. Greenaway, C. Self, M. S. Kim, and J. Knolle, Simple mitigation of global depolarizing errors in quantum simulations, Phys. Rev. E **104**, 035309 (2021).

[36] C. Schön, E. Solano, F. Verstraete, J. I. Cirac, and M. M. Wolf, Sequential Generation of Entangled Multiqubit States, Phys. Rev. Lett. **95**, 110503 (2005).

[37] A. Peruzzo, J. McClean, P. Shadbolt, M.-H. Yung, X.-Q. Zhou, P. J. Love, A. Aspuru-Guzik, and J. L. O'Brien, A variational eigenvalue solver on a photonic quantum processor, Nat. Commun. **5**, 4213 (2014).

[38] S.-H. Lin, R. Dilip, A. G. Green, A. Smith, and F. Pollmann, Real and imaginary-time evolution with compressed quantum circuits, PRX Quantum **2**, 010342 (2021).

[39] M. C. Bañuls, D. Pérez-García, M. M. Wolf, F. Verstraete, and J. I. Cirac, Sequentially generated states for the study of two-dimensional systems, Phys. Rev. A **77**, 052306 (2008).

[40] M. A. Levin and X.-G. Wen, String-net condensation: A physical mechanism for topological phases, Phys. Rev. B **71**, 045110 (2005).

[41] O. Buerschaper, M. Aguado, and G. Vidal, Explicit tensor network representation for the ground states of string-net models, Phys. Rev. B **79**, 085119 (2009).

[42] Z.-C. Gu, M. Levin, B. Swingle, and X.-G. Wen, Tensor-product representations for string-net condensed states, Phys. Rev. B **79**, 085118 (2009).

[43] E. Grant, M. Benedetti, S. Cao, A. Hallam, J. Lockhart, V. Stojevic, A. G. Green, and S. Severini, Hierarchical quantum classifiers, npj Quantum Inf. **4**, 65 (2018).

[44] I. Cong, S. Choi, and M. D. Lukin, Quantum convolutional neural networks, Nat. Phys. **15**, 1273 (2019).

[45] J. Biamonte, P. Wittek, N. Pancotti, P. Rebentrost, N. Wiebe, and S. Lloyd, Quantum machine learning, Nature (London) **549**, 195 (2017).

[46] A. Kay, Tutorial on the quantikz package, arXiv:1809.03842.